PHYSICAL REVIEW FLUIDS **5**, 113504 (2020)

Heat transfer scaling in natural convection with shear due to rotation

R. Vishnu and A. Sameen[*]
Department of Aerospace Engineering, Indian Institute of Technology Madras, Chennai 600036, India

(Received 26 May 2020; accepted 23 October 2020; published 16 November 2020)

Heat transport in natural convection commonly encountered in natural and engineering flows is affected by buoyancy forces and shear. The effect of rotational shear on heat transport is examined here. Direct numerical simulation of Rayleigh-Bénard convection (RBC) with a rotating lid is performed at various rotation Reynolds numbers (Re) and Rayleigh numbers (Ra). The simulations are done for a range Ra $\in [2 \times 10^3, 2 \times 10^7]$ and Re $\in [300, 3000]$. The rotating lid induces a shear into the flow resulting in two prominent flow regimes: a rotation-dominated (RD) regime and a convection-dominated (CD) regime. The RD and CD regimes are identified based on the heat transport scaling exponent of Ra. The flow topology in these two regimes is distinct, with the CD flow showing more RBC-like flow structures while the RD regime shows a central axial vortex flow. The variations of boundary layer thickness with Ra and Re also demonstrate the regimes. A parameter χ(Ra,Re) is developed to demarcate the two regimes.

DOI: 10.1103/PhysRevFluids.5.113504

I. INTRODUCTION

Rotating Rayleigh-Bénard convection in the presence of a Coriolis force is a canonical model to study astro- and geophysical flow phenomena such as convection in planetary atmospheres and deep ocean convection [1–3]. However, in most engineering flows and some geophysical scenarios, the Coriolis force is negligible compared to other forces such as buoyancy and shear. Examples include flame stabilization mechanisms in swirl combustors and cyclostrophic balance in tornadolike vortices where the pressure gradient balances the centrifugal force [1,4]. Photospheric vortex flows, associated with solar convection, and chromospheric swirls resembling supertornadoes are suggested to be mechanisms leading to corona heating in the sun [5–7]. Such a myriad of astrophysical, geophysical, and engineering flows involving interaction between vortex flows and buoyancy motivate us to characterize the dynamics due to a competing shear-buoyancy force pair.

In this paper, we investigate the unexplored scaling laws for heat transfer in Rayleigh-Bénard convection (RBC) with shear due to rotation. We identify the existence of mainly two flow regimes, and we also propose a criterion to demarcate these regimes. In our simulations, a swirl is generated by providing rotation about the wall normal axis to a heated/cooled surface. An axial vortex flow established by rotating the lid of a cylindrical container filled with fluid is the model system used in this paper. Literature on this flow, namely the Vogel-Escudier flow [8,9], focuses on a flow phenomenon referred to as a vortex breakdown [10–13], a paradigm for tornadoes [14–16]. The effect of buoyancy due to thermal gradients on a vortex breakdown [17,18] is relatively less investigated. The variations in heat transport for a stable thermal stratification with top lid rotation were examined for a limited range of parameters in Refs. [19,20], where suppression of a vortex breakdown bubble with increasing stratification was reported. The heat transport scaling in an

---

[*] sameen@ae.iitm.ac.in

unstable thermal stratification, however, is not known, which is the focus of this study, and it is different from RBC with background rotation [3,21–24].

There exists a vast literature on heat transport scaling laws in RBC [25–30] relating the Nusselt number Nu, defined as the ratio of the total heat flux to the conductive heat flux, and the Rayleigh number Ra, a measure of the buoyancy force. A power-law relation $\mathrm{Nu} \sim \mathrm{Ra}^n$, where the exponent n is between $2/7$ and $1/3$, is most commonly observed in computations and experiments of RBC. In the presence of external forcing, the functional form of the Nu-Ra relation is modified as $\mathrm{Nu} = f(\mathrm{Ra}, \mathrm{Re})$, where the Reynolds number Re is the ratio of the external forcing to the viscous force. In the present study, we examine top lid rotating Rayleigh-Bénard convection or thermally unstable top lid rotating Vogel-Escuider flow.

II. GOVERNING EQUATIONS AND NUMERICAL SETUP

We numerically investigate heat transport in RBC in a cylindrical domain with radius R and height H, with the cold top lid rotating with angular velocity Ω, keeping the sidewalls and bottom lid stationary. The nondimensional Navier-Stokes and energy equations in the polar cylindrical form under incompressible, Boussinesq approximations are

$$\frac{D\vec{V}}{Dt} = -\nabla p + \frac{\nabla^2 \vec{V}}{\left(\Pi\,\mathrm{Re} + \sqrt{\frac{\mathrm{Ra}}{\mathrm{Pr}}}\right)} + \frac{\mathrm{Ri}}{\left(1+\sqrt{\mathrm{Ri}}\right)^2} T\hat{z}, \tag{1}$$

$$\frac{DT}{Dt} = \left(\frac{1}{\Pi\,\mathrm{Re}\,\mathrm{Pr} + \sqrt{\mathrm{Ra}\,\mathrm{Pr}}}\right)\nabla^2 T, \tag{2}$$

where $\vec{V} = \{u_r, u_\theta, u_z\}$ is the velocity field, p is the pressure, T is temperature, and D/Dt is the total derivative. For nondimensionalization, the length scales as H and velocity scales as $u_0 = R\Omega + \sqrt{g\beta\Delta\Theta H}$ to accommodate the effects of both lid rotation and heating. The pressure is scaled by ρu_0^2. The temperature is nondimensionalized as $T = (\Theta - \Theta_c)/\Delta\Theta$, Θ_c is the dimensional temperature of the cold (top) plate, and $\Delta\Theta$ is the temperature difference between hot and cold plates. Here β is the isobaric thermal expansion coefficient of the fluid, and g is the acceleration due to gravity. The computational domain is shown in Fig. 1, along with the axis of rotation of the top plate; the coordinate system is fixed with the origin at the center of the stationary bottom wall.

The relevant nondimensional parameters are the aspect ratio, $\Pi = H/R$, the Reynolds number, $\mathrm{Re} = \Omega R^2/\nu$, the Rayleigh number, $\mathrm{Ra} = g\beta\Delta\Theta H^3/(\nu\alpha)$, and the Prandtl number, $\mathrm{Pr} = \nu/\alpha$, where ν is the kinematic viscosity and α is the thermal diffusivity of the fluid. In this paper, $\Pi = 2.5$ and $\mathrm{Pr} = 0.7$ are used for all the computations. The Richardson number, Ri, is defined as $\mathrm{Ri} = g\beta\Delta\Theta H/(\Omega^2 R^2) = \mathrm{Ra}/(\mathrm{Re}^2\Pi^2\mathrm{Pr})$. Rayleigh-Bénard convection as $\mathrm{Re} \to 0$ and Vogel-Escudier flow as $\mathrm{Ra} \to 0$ can be retrieved from Eqs. (1) and (2). The boundary conditions are as follows: at $z = 1$ (top lid), $u_r = u_z = 0$, $u_\theta = r/R(1 + \sqrt{\mathrm{Ri}})$, $T = 0$; at $z = 0$ (bottom lid), $u_r = u_z = u_\theta = 0$, $T = 1$; and at $r = R/H$ (side wall), $u_r = u_z = u_\theta = 0$, $\partial T/\partial r = 0$. The governing equations are solved using the fractional step finite-difference method on a staggered grid. Details of the numerical scheme are discussed in [31,32], implemented for Rayleigh-Bénard convection by [33,34], and extended for stratified/unstratified Vogel-Escudier flow by [35–37].

III. RESULTS AND DISCUSSION

A. Rotation influenced Nusselt number

The Nusselt number is defined as

$$\mathrm{Nu} = 1 + \sqrt{\mathrm{Ra}\,\mathrm{Pr}}\langle u_z T\rangle + \mathrm{Re}\,\mathrm{Pr}\Pi\langle u_z T\rangle, \tag{3}$$

accommodating the effect of convection heat transfer and rotation of the lid. The symbol $\langle\cdot\rangle$ denotes time and volume average. Table I shows a sample grid sensitivity study for $\mathrm{Ra} = 2 \times 10^7$; we take

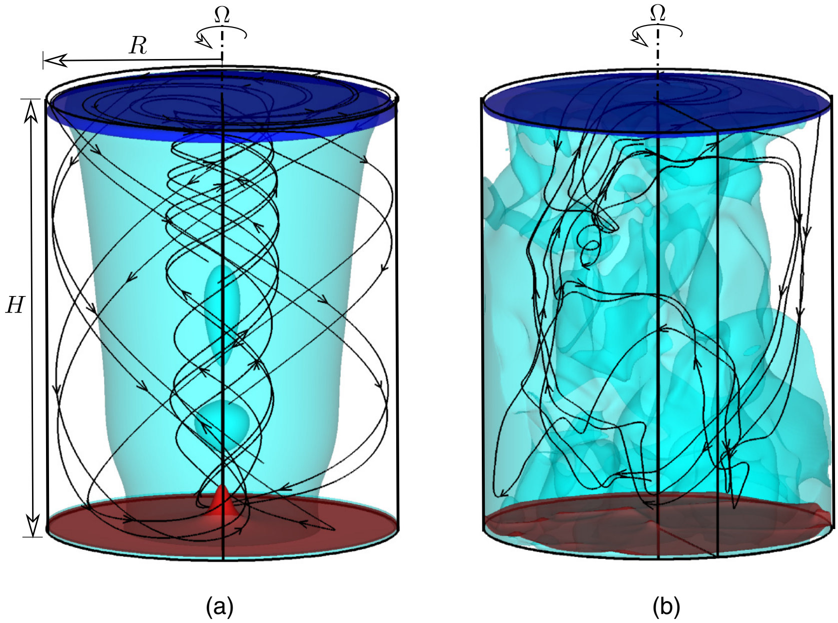

FIG. 1. Instantaneous isosurfaces of u_z and T with the streamlines (black) at the two regimes for Re = 2200. At (a) $\mathrm{Ra} = 2 \times 10^4$ (RD), streamlines swirl around the axis, a recirculation called a vortex breakdown bubble is shown as isosurface $u_z = 0$ (cyan); and (b) $\mathrm{Ra} = 2 \times 10^7$ (CD), the streamlines form RBC-like convection rolls. Temperature isosurfaces at $T = 0.9$ (red) and 0.05 (blue) indicate hot plumes at the bottom and cold plumes at the top for the two regimes. The direction of the top lid rotation is also indicated.

257 × 156 × 385 for our computations in this paper. The isocontour of $u_z = 0$, as well as $T = 0.9$ and 0.05, are shown in cyan, red, and blue, respectively, in Fig. 1. Two topologically different cases at Re = 2200—(a) at $\mathrm{Ra} = 2 \times 10^4$ and (b) at $\mathrm{Ra} = 2 \times 10^7$—are shown. Instantaneous streamlines are also plotted. Figure 1(a) corresponds to a situation in which the effect of Re dominates. This flow behavior is distinct from that at a higher Ra where the convection rolls form, as shown in Fig. 1(b). The present paper explores this shift in the dynamics in detail.

The Nusselt number evaluated at each instant [Eq. (3) without time-averaging] is plotted against time in Fig. 2. Figures 2(a) and 2(b) show Nu versus t for various Ra at Re = 800 and 3000, respectively. At higher Re, the flow heat transport is assisted by the rotation, showing an increase in Nu compared to lower Re. At large Ra, the Nu signal suggests turbulent flow similar to RBC. In the subsequent plots, the time-averaged value of the Nusselt number is reported. The sample values for statistical error in evaluating the mean are shown in the resolution check; see Table I.

At Ra = 0, Eq. (3) reduces to $\mathrm{Nu}_{\mathrm{Ra}=0} = 1 + \mathrm{Re}\,\mathrm{Pr}\Pi\langle u_z T\rangle$. It may be noted that Ra = 0 implies that buoyancy force is neglected, and the boundary conditions suggest a passive thermal gradient.

TABLE I. Nusselt number Nu and the number of grid points inside the bottom thermal boundary layer, shown for three different grid resolutions at $\mathrm{Ra} = 2 \times 10^7$, Re = 3000. The time averaging for Nu is done over ≈500 nondimensional times.

$N_\theta \times N_r \times N_z$	dt	Nu	Grid points
193 × 117 × 289	0.001	22.95 ± 0.09	12
257 × 156 × 385	0.001	22.97 ± 0.51	15
321 × 195 × 482	0.001	22.59 ± 0.31	19

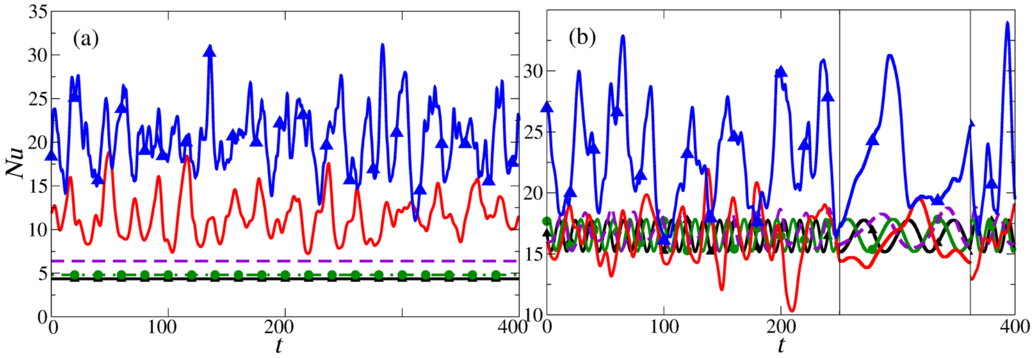

FIG. 2. Nu plotted against nondimensional time t for (a) Re = 800 and (b) Re = 3000. The corresponding Ra are ▲— Ra $= 0$, ●— Ra $= 2 \times 10^4$, - - - Ra $= 2 \times 10^5$, — Ra $= 2 \times 10^6$, and ▲— Ra $= 2 \times 10^7$. The inset in (b) shows the zoomed signal with a window size of 40 time units.

The heat transport at Ra = 0, i.e., $\mathrm{Nu}_{\mathrm{Ra}=0}$, is plotted against Re in Fig. 3. The dashed line in the plot is the least-squares fit curve. It indicates a correlation $\mathrm{Nu}_{\mathrm{Ra}=0} \sim \mathrm{Re}^{1.1}$, and it shows the contribution of the rotation component in the heat transport.

B. Transition Rayleigh number

The dependence of Nu on Ra for various Re is plotted in Fig. 4 in log scale. For any given Re, as Ra is increased, Nu remains almost constant but with a small slope until a transition Rayleigh number, Ra_t. Upon further increase in Ra ($> \mathrm{Ra}_t$), the slope of the curve changes to a steeper one, coinciding with the slope for RBC (Re = 0). The transition Rayleigh number Ra_t is identified in three different ways, as discussed below. (i) Method-1 defines Ra_t as the Ra at which the slope for various Re locks on to the steeper RBC slope.

Following this definition, we compute Ra_t as the lowest Ra when the Nu for a given Re attains Nu for Re = 0 (RBC) case, which is shown as a dashed black line in Fig. 4. This change in slope is observed for all Re, with an increase of Ra_t with Re. For lower Re, the transition is sharp, and

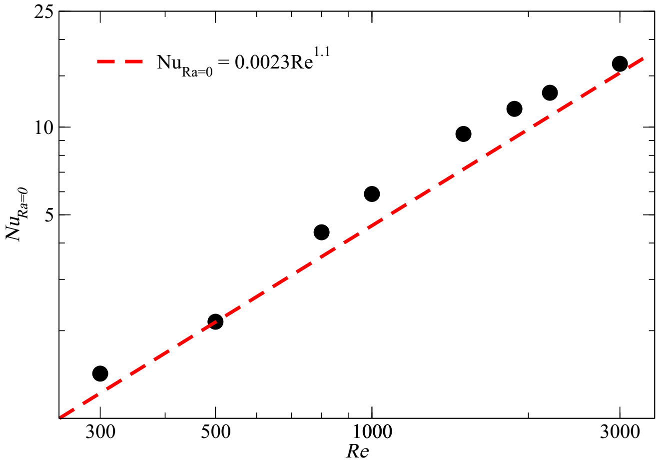

FIG. 3. Variation of $\mathrm{Nu}_{\mathrm{Ra}=0}$ for various Re. Note that Ra = 0 implies that buoyancy force is neglected, and the boundary conditions $T = 0$ at the top and $T = 1$ at the bottom plates ensure a passive thermal gradient in the domain. The heat transfer is due to swirling motion (Re), and the Nu follows a power law $\sim\mathrm{Re}^{1.1}$.

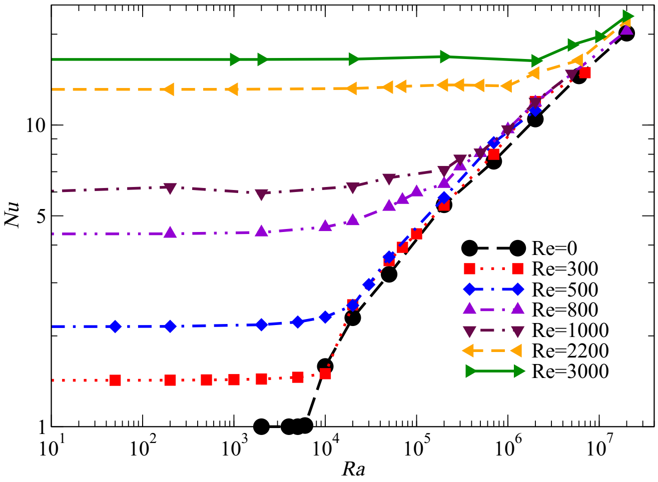

FIG. 4. Variation of Nu with Ra for various Re. Transition from rotational- to convection-dominated regimes is evident from the change in slopes for various Re.

for higher Re the transition is gradual. Hence this method is very appropriate for low Re cases. (ii) In method-2, we first draw a straight line connecting Nu for RD cases (Nu $\sim$ Ra^0) for a particular Re. For this, the initial few Nu values in the RD regime are chosen. Then Ra$_t$ is identified as the Ra at the intersection of this line with Nu $\sim$ Ra$^{0.33}$ (the final few Nu values in the CD regime are chosen) for that Re. Since the transition from RD to CD is gradual for high Re cases, this method is appropriate for large Re cases. For computing the slope (or exponent) of Ra$_t$-Re scaling, we used only large Re cases. (iii) Method-3 is similar to method-2, and in method-3 we define the Ra$_t$ as the Ra at the intersection of the straight line connecting Nu for a particular Re in the RD regime (Nu $\sim$ Ra^0) with RBC scaling of Nu $\sim$ Ra$^{0.33}$. All of the above definitions are used to find Ra$_t$, which is shown in Fig. 5. The red circles in Fig. 5 are Ra$_t$ identified from method-1, blue squares

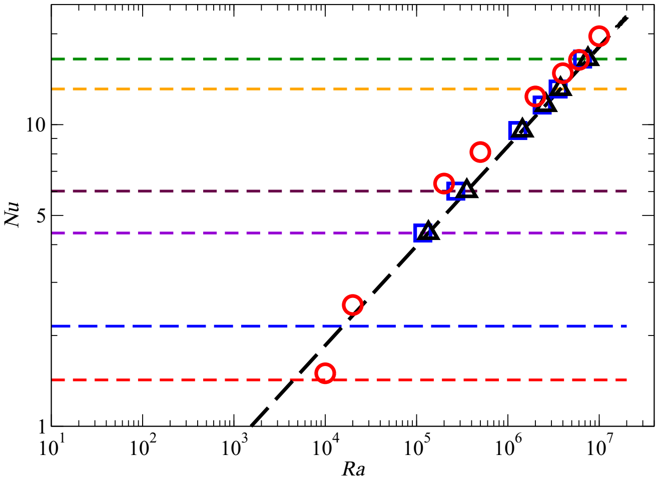

FIG. 5. Ra$_t$ is identified using three different ways. The red circle is the Ra$_t$ obtained from method-1, the square from method-2, and the triangle from method-3. All horizontal lines are joining the Nu in the RD regime for various Re as given Fig. 4. The dashed black line is RBC scaling Nu $\sim$ Ra$^{0.33}$.

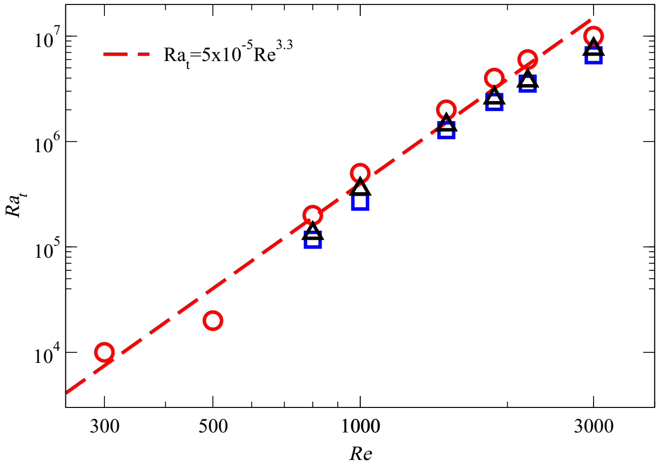

FIG. 6. Variation of transitional Rayleigh number Ra_t with Re. Ra_t identified from method-1 (red circles) is used to get the least-squares fit (dashed line) given as $\mathrm{Ra}_t = 5 \times 10^{-5}\mathrm{Re}^{3.3}$. Blue squares and black triangles are Ra_t from method-2 and method-3, respectively, and the deviation from least-squares fit is shown as the error in evaluating the exponent.

are the Ra_t using method-2, and triangles are from method-3. The black straight line is $\mathrm{Nu} \sim \mathrm{Ra}^{0.33}$, which is shown for comparison. The deviations of Ra_t computed from various methods are small, as seen in Fig. 5. Without losing generality, we adopt Ra_t from method-1 for further analysis in the paper. In Fig. 6, the Ra_t obtained from various methods are plotted. The deviation from the least-squares fit of method-2 from method-1 is shown as the error in exponent while computing Ra_t, given as

$$\mathrm{Ra}_t \sim \mathrm{Re}^p, \quad \text{where } 3.12 \leqslant p \leqslant 3.3. \tag{4}$$

In Fig. 4, the Nu has two distinct slopes, suggesting two regimes of the flow. The smaller slope indicates a rotation-dominated regime (RD), while the steeper slope indicates a convection-dominated regime (CD). At low Ra, due to the rotation, the transport of heat is dominated by the swirl flow, and beyond Ra_t, the mode of heat transport changes to thermal convection. It may be noted that for classical RBC there is no transition from RD to CD since the flow is always CD. In such a case, $\mathrm{Ra}_t = 0$ as defined in Eq. (4).

A correlation between Nu and Ra is obtained by normalizing Nu by $\mathrm{Nu}_{\mathrm{Ra}=0}$ and Ra by Ra_t. For various combinations of Ra and Re values, the normalized Nusselt number is plotted against $\mathrm{Ra}/\mathrm{Ra}_t$ in Fig. 7. The existence of RD and CD regimes is clear from the occurrence of two distinct slopes in the log-log plot. The circles are RD data points from the smaller slope of Fig. 4, while upper triangles are from the steeper slope.

In the figure, the lower bound of the normalized Nusselt number for RD is unity by definition [Eq. (3)]. The upper bound is obtained by the curve fitting of maximum values for all $\mathrm{Ra}/\mathrm{Ra}_t$, which is also shown in the figure. At around $\mathrm{Ra}/\mathrm{Ra}_t = 1$, the cluster of points indicates a transition from RD to CD. In the CD regime, the flow asymptotically goes to Rayleigh-Bénard convection, and heat transport dependence on Ra attains the power law $\mathrm{Ra}^{0.33}$. We derive from the best-fit curves the correlation $\mathrm{Nu} = f(\mathrm{Ra,Re})$ in the two regimes as follows:

$$\mathrm{Nu} = \begin{cases} 0.074\mathrm{Re}^{0.05}\mathrm{Ra}^{0.33} & \text{for CD,} \\ 0.0023\mathrm{Re}^{1.1} + 35.28\mathrm{Ra}\mathrm{Re}^{-2.2} & \text{upper limit of RD,} \\ 0.0023\mathrm{Re}^{1.1} & \text{lower limit of RD.} \end{cases} \tag{5}$$

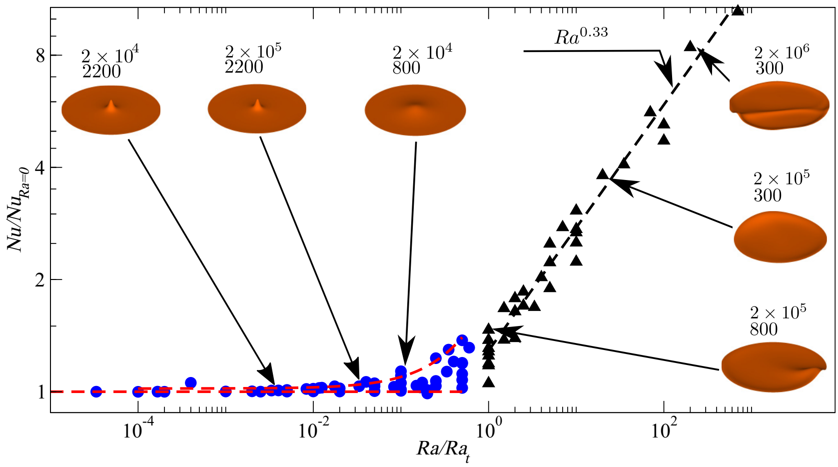

FIG. 7. Normalized Nusselt number plotted against the normalized Rayleigh number. The circles indicate rotation dominated while the upper triangles indicate convection-dominated regimes, identified from Fig. 4. The red dashed lines indicate upper- and lower-bound values for the RD regime. The black dashed line indicates RBC correlation Nu $\sim$ Ra$^{0.33}$, which is attained in the CD regime. The insets show plumes identified by the temperature isosurface value of 0.9 for various Ra and Re, indicated by the top and bottom values in the insets, respectively. Note the distinct plume shapes in the RD and CD regimes.

Shown in the insets of Fig. 7 are some sample temperature isosurfaces ($T = 0.9$) to indicate the instantaneous plume structure near the bottom hot plate. The plume structures are distinctly different in the two regimes. In the RD regime, there is a central axial plume carrying heat as against line plumes in the CD regime. The single upwelling in the RD regime is caused by the hot fluid converging at the axis due to the swirl at the bottom [9]. The CD regime features line plumes along the sides or in the interior that are similar to those observed for Rayleigh-Bénard convection [38–40]. The increased Nu in the CD regime is attributed to the large surface area of these line-plumes associated with high Ra (similar to RBC) as compared to the single plume at the axis observed in the RD regime. The plume structure in these regimes is corroborated with the flow patterns, as shown in Fig. 8. The two regimes are shown using instantaneous two-dimensional (2D) streamlines projected to the central r-z plane, drawn over slices of temperature contours for Re = 300 and 3000. From the left subplot to the right, Ra increases, and there is a transformation from a central vortex pattern (RD) to convection large-scale circulation (CD). The transition from RD to CD is characterized by the topological change from axial vortex dominated to convection roll dominated flow. It is observed that for Re = 300, at larger Ra, as in subplot (c), the flow is dominated by a single large-scale circulation, similar to RBC [28,41,42].

C. Thermal boundary layers

We examine next the scaling between the thermal boundary-layer thickness and Nu in both regimes, which for RBC is of the form $\delta_\theta \sim 1/\mathrm{Nu}$ [30]. Figure 9 shows the temperature profiles averaged over time, r, and θ direction at Re = 2200 for various Ra. The temperature at $z = 0.5$ for pure RBC is $T_c = 0.5$, and from Fig. 9 the presence of top lid rotation brings down the cylinder midtemperature. The thermal boundary-layer thickness, δ_θ, is an important quantity that can be estimated from temperature profiles. The δ_θ is calculated as the height from the plate where the linear extrapolation of the mean temperature profile at the bottom/top plate intersects the temperature at the midheight, T_c [43]; a schematic is shown in the inset of Fig. 9. The δ_θ computed for the top and bottom boundary layers (δ_{θ_T} and δ_{θ_B}) for Re = 2200 is shown in Fig. 10. As Ra increases, the δ_{θ_B} decreases as noted for RBC [44]. Also evident is the asymmetry in the boundary-layer thickness

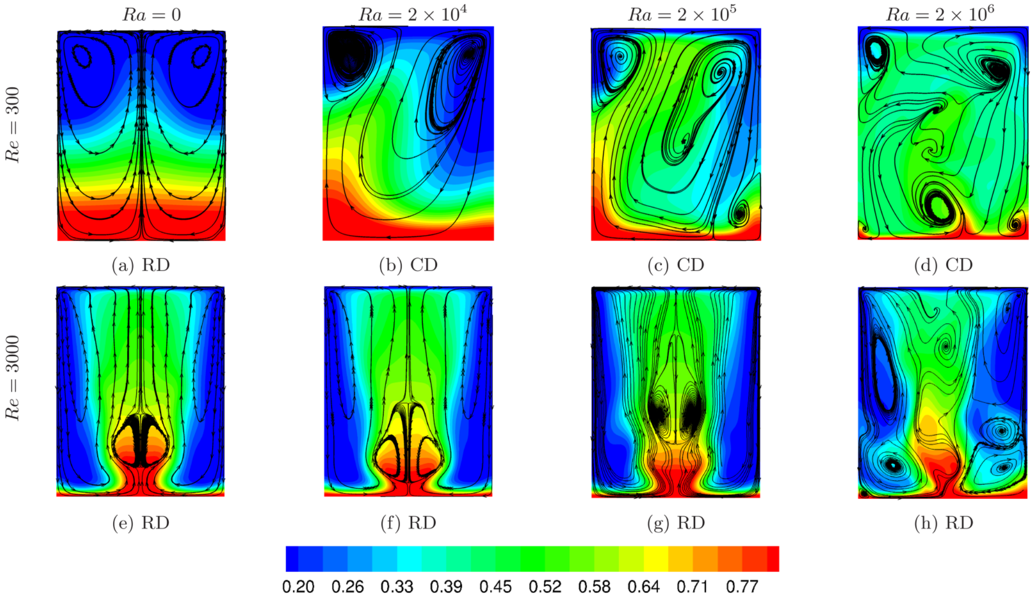

(a) RD (b) CD (c) CD (d) CD

(e) RD (f) RD (g) RD (h) RD

FIG. 8. The temperature contours with streamlines for various Ra and Re. The streamline patterns show the transition from RD to CD (from left to right) with the increase in Ra. Large-scale circulation, which is a signature of RBC observed in the convection-dominated regime. Also seen are the axial vortex and vortex breakdown bubbles in the RD regimes [far left, (e) and (f)].

due to rotation on the top plate. In RBC, within the Boussinesq assumption, the top and bottom boundary-layer thicknesses are equal [45,46]. Here, as the flow moves toward CD from RD, $\delta_{\theta_T}/\delta_{\theta_B}$ should approach unity. The low Ra cases shown in Fig. 9 are RD regimes and move toward CD as the Ra increases. The center temperature progressively increases toward the RBC value of $T_c = 0.5$

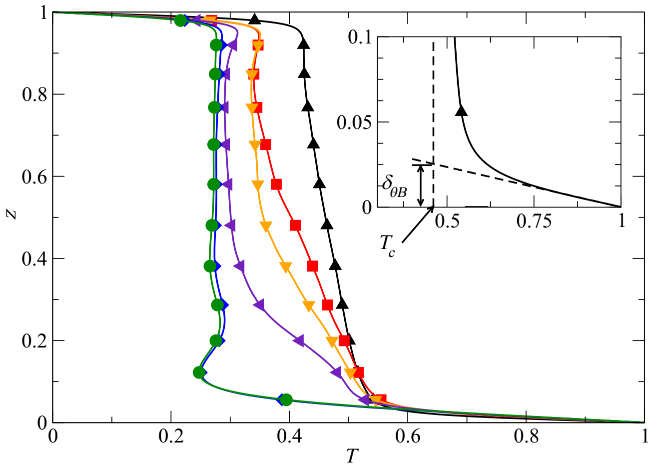

FIG. 9. The temperature profiles for varying Ra at Re = 2200. The corresponding Ra are ●— Ra = 2 × 10^4, ◆— Ra = 2 × 10^5, ◀— Ra = 2 × 10^6, ▼— Ra = 4 × 10^6, ■— Ra = 6 × 10^6, and ▲— Ra = 2 × 10^7. The inset shows a schematic of the thermal boundary-layer thickness. The height at which the linear extrapolation at the bottom plate intersects with T_c is defined as δ_{θ_B}.

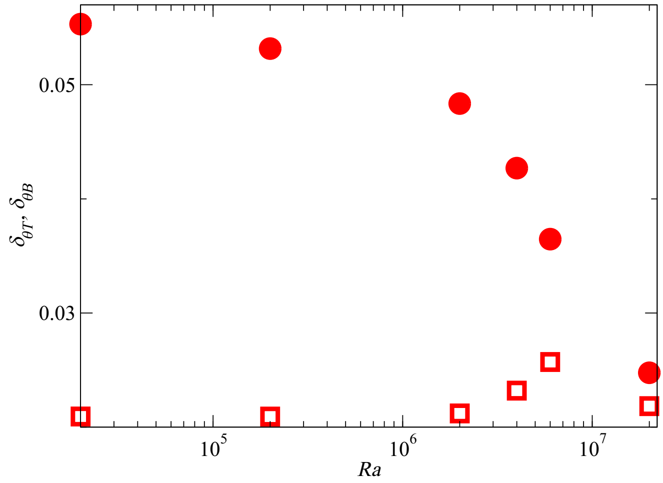

FIG. 10. The thermal boundary layer thickness δ_θ for the cases shown in Fig. 9. The δ_{θ_T} (square) and δ_{θ_B} (circle) at Re = 2200 for various Ra.

as the flow shifts from the RD to the CD regime. Next, the cases of RD and CD are segregated, and the δ_θ is plotted. The δ_θ computed from numerical simulations for the CD regime is shown in Fig. 11(a). In the CD regime, at higher Ra, δ_{θ_T} and δ_{θ_B} are approaching equal values as in RBC. In the figure, 1/Nu is also plotted for comparison in red filled circles. From RBC it is known that $\delta_\theta \sim 1/\mathrm{Nu}$. The dashed line is shown for comparison, indicating that the correlation $\delta_\theta \sim \mathrm{Ra}^{-0.33}$ [see Eq. (5)]. Similarly, the computed values of δ_θ and 1/Nu for the RD regime are plotted in Fig. 11(b). The boundary-layer thickness is different here, as discussed earlier due to asymmetry created by top lid rotation. The source of the heat is from the bottom plate, and we discuss the bottom thermal boundary-layer scaling. For the RD regime, $\delta_{\theta_B} \sim \mathrm{Re}^{-1.1}$, the scaling from Eq. (5) is plotted for comparison.

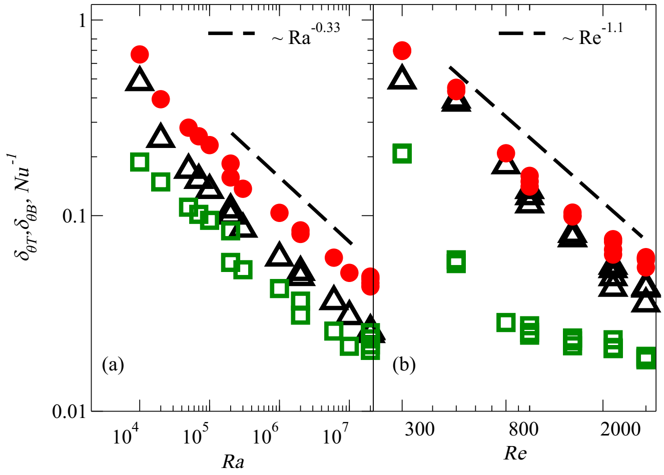

FIG. 11. Variation of the bottom thermal boundary layer thickness, δ_{θ_B} (black open triangles), for varying Ra and Re, compared with the inverse of the Nusselt number (red filled circles). The subplot (a) has all the data points from the CD regime while (b) has all the data points from the RD regime. Open green squares are top thermal boundary layer thickness, and the dashed lines indicate the slopes with power-law exponents as shown.

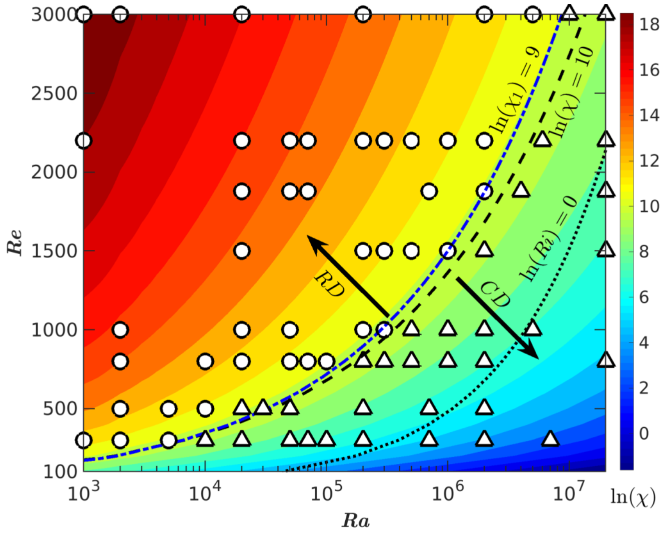

FIG. 12. The contour plot of the nondimensional number, χ, plotted as $\ln(\chi)$. Data from the simulations are plotted over the contour. The circles correspond to RD and triangles correspond to CD. The thick line demarcates the two regimes at $\ln(\chi) = 10$. The contour line of $\ln(\chi_1) = 9$ is shown to include the effect of error in evaluating Ra_t. For comparison, $\mathrm{Ri} = 1$ is plotted to show that the demarcation between the regimes is captured better by χ.

D. A parameter identifying rotation and convection regimes

Similar to rotating RBC [21], the global heat transfer is determined by the dynamics in the boundary layer in both regimes. According to the definition of Ra_t, at the point of transition from RD to CD, where $\mathrm{Ra} = \mathrm{Ra}_t$, scaling of both regimes overlaps. This also implies that the above scaling matches for both RD and CD regimes in the overlap region, leading to (i.e., at $\mathrm{Ra}/\mathrm{Ra}_t \sim 1$)

$$\mathrm{Ra}^{-0.33} \sim \mathrm{Re}^{-1.1}. \tag{6}$$

From the above equation, upon substitution, we get $\mathrm{Ra}_t \sim \mathrm{Re}^{3.3}$.

Finally, we heuristically devise a parameter

$$\chi = \frac{\mathrm{Ra}_t}{\mathrm{Ra}} = \frac{\mathrm{Re}^{3.3}}{\mathrm{Ra}} \tag{7}$$

to demarcate the RD and CD regimes. Noting that there is an error band in identifying Ra_t, we also determine $\chi_1 = \mathrm{Re}^{3.12}/\mathrm{Ra}$. The contour of $\ln(\chi)$ is plotted in the phase diagram of Ra versus Re in Fig. 12. As in Fig. 7, the circles represent RD regimes and triangles represent CD regimes. The region below the dashed line [$\ln(\chi) = 10$] is seen to be populated by CD regimes, while the region above is by RD regimes. The demarcation between the regimes is well captured by $\ln(\chi) = 10$. The contour of $\ln(\chi_1) = 9$ is also shown in the plot, thus the error in the determination of Ra_t is shown as a small region of transition [between $\ln(\chi_1) = 9$ and $\ln(\chi) = 10$], instead of a sharp transition jump. In Fig. 12, $\mathrm{Ri} = 1$ contour is also plotted for comparison, $\mathrm{Ri} \gg 1$ suggests buoyancy-dominated flow, while $\mathrm{Ri} \ll 1$ suggests shear-dominant flow. However, in the present problem, we find that χ represents better the transition between the regimes.

Interestingly, with the prefactor for Ra_t scaling, from Eq. (4), these demarcation values may change; nevertheless, χ is a useful parameter to identify the regimes. The transition is not a sharp jump from the RD to the CD regime. Figure 13 shows the χ values for a set of cases that includes the near-transition region. In the figure, from top to bottom is increasing Re and left to right is increasing Ra. It is evident that for cases close to $\ln(\chi) = 10$, the flow has features of both RD and CD

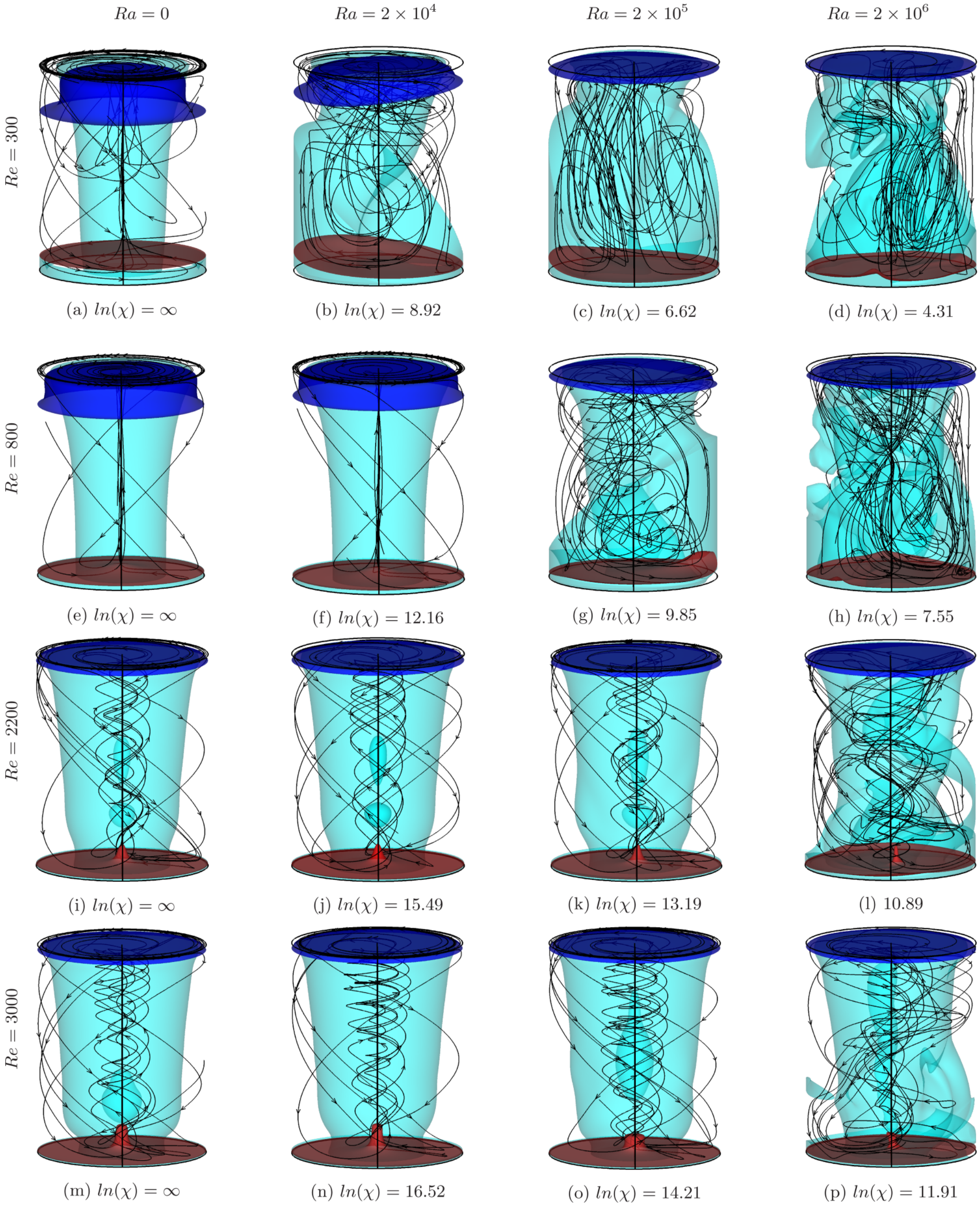

(a) $ln(\chi) = \infty$ (b) $ln(\chi) = 8.92$ (c) $ln(\chi) = 6.62$ (d) $ln(\chi) = 4.31$

(e) $ln(\chi) = \infty$ (f) $ln(\chi) = 12.16$ (g) $ln(\chi) = 9.85$ (h) $ln(\chi) = 7.55$

(i) $ln(\chi) = \infty$ (j) $ln(\chi) = 15.49$ (k) $ln(\chi) = 13.19$ (l) 10.89

(m) $ln(\chi) = \infty$ (n) $ln(\chi) = 16.52$ (o) $ln(\chi) = 14.21$ (p) $ln(\chi) = 11.91$

FIG. 13. Instantaneous isosurfaces of u_z and T along with streamlines for various Ra and Re. For the RD regime, $\ln(\chi) \gtrsim 10$, streamlines swirl around the axis and form a recirculation called a vortex breakdown bubble [37], which is shown as isosurface $u_z = 0$ (cyan). For the CD regime $\ln(\chi) \lesssim 10$, the streamlines form RBC-like convection rolls. The temperature isosurface at $T = 0.9$ (red) and 0.05 (blue) indicates hot plumes at the bottom and cold plumes at the top for the two regimes. A single axial plume dominates for the RD regime while line plumes dominate for the CD regime.

regimes, namely an axial plume and large-scale circulation, respectively. From the simulation, with the definition of Ra_t, we obtain $\ln(\chi) = 10$ to demarcate the RD and CD regimes. The parameter χ has the form of the shear parameter, $S = 2\,\mathrm{Re}^3/\mathrm{Ra}$, recently proposed for RBC [47], which indicates the relative strength of linear shear and buoyancy effects. There is nevertheless a need to elucidate the physical meaning of the exponent of Re.

IV. CONCLUSION

The paper discusses rotation-induced shear effects on Rayleigh-Bénard convection and heat transport scaling. The top lid of the convection cell is rotated and based on the rotational speed and buoyancy, there exist two flow regimes, namely rotation-dominated and convection-dominated. The Nusselt number depends on the Reynolds number and the Rayleigh number of the flow, and the newly identified parameter χ can be used as a criterion to identify RD [$\ln(\chi) > 10$] and CD [$\ln(\chi) < 10$] regimes.

ACKNOWLEDGMENTS

The authors acknowledge the Virgo cluster at IIT Madras for computations done in this paper. Personal communications with B. A. Puthenveettil, Edgar Knobloch, and Stephan Stellmach were also helpful.

---

[1] S. Horn and J. M. Aurnou, Regimes of Coriolis-Centrifugal Convection, Phys. Rev. Lett. **120**, 204502 (2018).

[2] J.-Q. Zhong, R. J. A. M. Stevens, H. J. H. Clercx, R. Verzicco, D. Lohse, and G. Ahlers, Prandtl-, Rayleigh-, and Rossby-Number Dependence of Heat Transport in Turbulent Rotating Rayleigh-Bénard Convection, Phys. Rev. Lett. **102**, 044502 (2009).

[3] R. E. Ecke and J. J. Niemela, Heat Transport in the Geostrophic Regime of Rotating Rayleigh-Bénard Convection, Phys. Rev. Lett. **113**, 114301 (2014).

[4] R. J. Trapp and R. Davies-Jones, Tornadogenesis with and without a dynamic pipe effect, J. Atmos. Sci. **54**, 113 (1997).

[5] S. Wedemeyer-Böhm, E. Scullion, O. Steiner, L. R. van der Voort, J. de La Cruz Rodriguez, V. Fedun, and R. Erdélyi, Magnetic tornadoes as energy channels into the solar corona, Nature (London) **486**, 505 (2012).

[6] J. A. Bonet, I. Márquez, J. S. Almeida, I. Cabello, and V. Domingo, Convectively driven vortex flows in the Sun, Astrophys. J. Lett. **687**, L131 (2008).

[7] A. Vögler, S. Shelyag, M. Schüssler, F. Cattaneo, T. Emonet, and T. Linde, Simulations of magneto-convection in the solar photosphere-equations, methods, and results of the MURaM code, Astron. Astrophys. **429**, 335 (2005).

[8] H. U. Vogel, *Experimentelle Ergebnisse Ueber die Laminare Stroemung in Einem Zylindrischen Gehaeuse mit Darin Rotierender Sceibe* (Max-Planck-Institut für Strömungsforschung, Göttingen, Bericht, 1968), Vol. 6.

[9] M. P. Escudier, Observations of the flow produced in a cylindrical container by a rotating endwall, Exp. Fluids **2**, 189 (1984).

[10] J. M. Lopez and A. D. Perry, Axisymmetric vortex breakdown. Part 3. Onset of periodic flow and chaotic advection, J. Fluid Mech. **234**, 449 (1992).

[11] G. L. Brown and J. M. Lopez, Axisymmetric vortex breakdown. Part 2. Physical mechanisms, J. Fluid Mech. **221**, 553 (1990).

[12] J. N. Sørensen and E. A. Christensen, Direct numerical simulation of rotating fluid flow in a closed cylinder, Phys. Fluids **7**, 764 (1995).

[13] F. Marques and J. M. Lopez, Precessing vortex breakdown mode in an enclosed cylinder flow, Phys. Fluids **13**, 1679 (2001).

[14] D. C. Lewellen and W. S. Lewellen, Near-surface intensification of tornado vortices, J. Atmos. Sci. **64**, 2176 (2007).

[15] R. Rotunno, The fluid dynamics of tornadoes, Annu. Rev. Fluid Mech. **45**, 59 (2013).

[16] R. J. Trapp, A clarification of vortex breakdown and tornadogenesis, Month. Weath. Rev. **128**, 888 (2000).

[17] C. H. Lee and J. M. Hyun, Flow of a stratified fluid in a cylinder with a rotating lid, Int. J. Heat Fluid Flow **20**, 26 (1999).

[18] H. J. Lugt and M. Abboud, Axisymmetric vortex breakdown with and without temperature effects in a container with a rotating lid, J. Fluid Mech. **179**, 179 (1987).

[19] W. N. Kim and J. M. Hyun, Convective heat transfer in a cylinder with a rotating lid under stable stratification, Int. J. Heat Fluid Flow **18**, 384 (1997).

[20] R. Iwatsu, Flow pattern and heat transfer of swirling flows in cylindrical container with rotating top and stable temperature gradient, Int. J. Heat Mass Transf. **47**, 2755 (2004).

[21] E. M. King, S. Stellmach, J. Noir, U. Hansen, and J. M. Aurnou, Boundary layer control of rotating convection systems, Nature (London) **457**, 301 (2009).

[22] Y. Liu and R. E. Ecke, Heat Transport Scaling in Turbulent Rayleigh-Bénard Convection: Effects of Rotation and Prandtl Number, Phys. Rev. Lett. **79**, 2257 (1997).

[23] J.-Q. Zhong and G. Ahlers, Heat transport and the large-scale circulation in rotating turbulent Rayleigh-Bénard convection, J. Fluid Mech. **665**, 300 (2010).

[24] K. Julien, S. Legg, J. McWilliams, and J. Werne, Rapidly rotating turbulent Rayleigh Bénard convection, J. Fluid Mech. **322**, 243 (1996).

[25] R. M. Kerr, Rayleigh number scaling in numerical convection, J. Fluid Mech. **310**, 139 (1996).

[26] B. Castaing, G. Gunaratne, F. Heslot, L. Kadanoff, A. Libchaber, S. Thomae, X.-Z. Wu, S. Zaleski, and G. Zanetti, Scaling of hard thermal turbulence in Rayleigh-Bénard convection, J. Fluid Mech. **204**, 1 (1989).

[27] R. Benzi, F. Toschi, and R. Tripiccione, On the heat transfer in Rayleigh-Bénard systems, J. Stat. Phys. **93**, 901 (1998).

[28] G. Ahlers, S. Grossmann, and D. Lohse, Heat transfer and large scale dynamics in turbulent Rayleigh-Bénard convection, Rev. Mod. Phys. **81**, 503 (2009).

[29] B. I. Shraiman and E. D. Siggia, Heat transport in high-Rayleigh-number convection, Phys. Rev. A **42**, 3650 (1990).

[30] S. Grossmann and D. Lohse, Scaling in thermal convection: a unifying theory, J. Fluid Mech. **407**, 27 (2000).

[31] R. Verzicco and P. Orlandi, A finite-difference scheme for three-dimensional incompressible flow in cylindrical coordinates, J. Comput. Phys. **123**, 402 (1996).

[32] R. Verzicco and R. Camussi, Transitional regimes of low-Prandtl thermal convection in a cylindrical cell, Phys. Fluids **9**, 1287 (1997).

[33] R. Verzicco and R. Camussi, Numerical experiments on strongly turbulent thermal convection in a slender cylindrical cell, J. Fluid Mech. **477**, 19 (2003).

[34] R. J. A. M. Stevens, R. Verzicco, and D. Lohse, Radial boundary layer structure and Nusselt number in Rayleigh-Bénard convection, J. Fluid Mech. **643**, 495 (2010).

[35] M. Sharma and A. Sameen, Axisymmetric vortex breakdown: A barrier to mixing, Phys. Scr. **94**, 054005 (2019).

[36] R. Vishnu and A. Sameen, Heat transport in rotating-lid Rayleigh-Bénard convection, Phys. Scr. **94**, 054004 (2019).

[37] M. Sharma and A. Sameen, On the correlation between vortex breakdown bubble and planar helicity in Vogel-Escudier flow, J. Fluid Mech. **888**, A6-1 (2020).

[38] B. A. Puthenveettil, G. S. Gunasegarane, Y. K. Agrawal, D. Schmeling, J. Bosbach, and J. H. Arakeri, Length of near-wall plumes in turbulent convection, J. Fluid Mech. **685**, 335 (2011).

[39] G. Zocchi, E. Moses, and A. Libchaber, Coherent structures in turbulent convection, an experimental study, Physica A **166**, 387 (1990).

[40] R. Verzicco and K. R. Sreenivasan, A comparison of turbulent thermal convection between conditions of constant temperature and constant heat flux, J. Fluid Mech. **595**, 203 (2008).

[41] H.-D. Xi, S. Lam, and K.-Q. Xia, From laminar plumes to organized flows: The onset of large-scale circulation in turbulent thermal convection, J. Fluid Mech. **503**, 47 (2004).

[42] T. Hartlep, A. Tilgner, and F. H. Busse, Large Scale Structures in Rayleigh-Bénard Convection at High Rayleigh Numbers, Phys. Rev. Lett. **91**, 064501 (2003).

[43] A. Belmonte, A. Tilgner, and A. Libchaber, Temperature and velocity boundary layers in turbulent convection, Phys. Rev. E **50**, 269 (1994).

[44] X.-Z. Wu and A. Libchaber, Non-Boussinesq effects in free thermal convection, Phys. Rev. A **43**, 2833 (1991).

[45] G. Ahlers, E. Brown, F. F. Araujo, D. Funfschilling, S. Grossmann, and D. Lohse, Non-Oberbeck-Boussinesq effects in strongly turbulent Rayleigh-Bénard convection, J. Fluid Mech. **569**, 409 (2006).

[46] A. D. Demou and D. G. E. Grigoriadis, Direct numerical simulations of Rayleigh-Bénard convection in water with non-Oberbeck–Boussinesq effects, J. Fluid Mech. **881**, 1073 (2019).

[47] P. P. Shevkar, G. S. Gunasegarane, S. K. Mohanan, and B. A. Puthenveettil, Effect of shear on coherent structures in turbulent convection, Phys. Rev. Fluids **4**, 043502 (2019).